Journal of Geophysical Research: Solid Earth

Supporting Information for

How do laboratory friction parameters compare with observed fault slip and geodetically derived friction parameters? Insights from the Longitudinal Valley Fault, Taiwan

S. A. M. den Hartog[1†], M. Y. Thomas[2], and D. R. Faulkner[1]

[1] Rock Deformation Laboratory, School of Environmental Sciences, University of Liverpool, Liverpool, United Kingdom.
[2] Institut des Sciences de la Terre de Paris, CNRS-UMR 7193, Sorbonne Université, Paris, France.
Corresponding author: Sabine den Hartog (s.den_hartog@hw.ac.uk)
[†]Now at: The Lyell Centre, Heriot-Watt University, Edinburgh, UK.

Contents of this file

Introduction

This Supporting Information provides 10 figures that are additional to those in the main manuscript. Figure S1 shows the long-term motion of the Coastal Range and Central Range blocks, the Static Coulomb stress changes and the inferred friction parameter. Figure S2 displays the three inversion models used in this study and Figure S3 gives the corresponding resolution maps of these models. Figure S4 shows results for the time series of slip derived from the inversion of the geodetic data. Figure S5 shows close-up portions of friction profiles annotated with the derived Rate and State Friction (RSF) parameters. Figure S6 shows the dip angle of the Longitudinal Valley Fault (LVF) with depth, as well as the assumed depth-profiles of effective normal stress and temperature. Figure S7 shows the corresponding (*a*-*b*) values and compares them with the experimentally derived (*a*-*b*) values. Figure S8 shows the RSF parameters of the additional friction experiments in which the effect of kaolinite was investigated. Finally, Figures S9 and S10 show Energy Dispersive X-Ray results for the samples with added and natural kaolinite.

Text S1. Inversion procedure - general consideration

Because of the very limited sensitivity of the data to slip at great depth, in each slip model the inversion is limited to the fault portion shallower than 26 km (corresponding to 15 cells along the downdip direction). The deeper part of the fault (not displayed in Figure S2) is assumed to slip at the long-term slip rate imposed by the relative block motion between the Central Range and Coastal Range (Figure S1a). Consistently, are included in the inversion only the GPS stations that could have recorded shallow slip displacement, i.e., stations that are at most ~30 km away from the fault trace. More details on the inversion procedure are provided in Thomas et al., (2014a).

Text S2. Secular Interseismic model

Because of the lack of data available for the period preceding the 2003 Chengkung earthquake, the published preseismic model of Thomas et al., (2014a) is poorly resolved. For this study, we decided to use instead the so-called "secular interseismic" model which gives the time-averaged pattern of slip rate on the LVF in the interseismic period. To compute this model, they inverted the GPS campaign measurements, the leveling data, the PS ALOS mean velocity, and the secular velocities determined with the continuous GPS and the creepmeter's timeseries. The latter was obtained from the least squares fitting of the time series with the following equation:

$$u^i(t) = u_o^i + v^i t + \sum_k h_k^i H(t - t_k) + \sum_k r_k^i H(t - t_k) \log\left(1 + \frac{(t - t_k)}{\tau}\right) + \sum_p \left(s_p^i \sin\left(\frac{2\pi t}{T_p}\right) + c_p^i \cos\left(\frac{2\pi t}{T_p}\right)\right)$$

where i = (north, east, and up), u_o is a constant offset, v_t correspond to the secular velocity, H is a Heaviside step function standing for coseismic displacement, t_k is the time at which the step occurs, and the Heaviside step function multiplied by the logarithmic function follows the postseismic relaxation with τ, the characteristic time constant. c_p and s_p corresponds to the coefficients to model the harmonic variations of period T_p. Annual and a semiannual period were considered. The linear parameters u_o^i, v^i, h_k^i, r_k^i, s_p^i, and c_p^i were estimated through a standard least square's inversion.

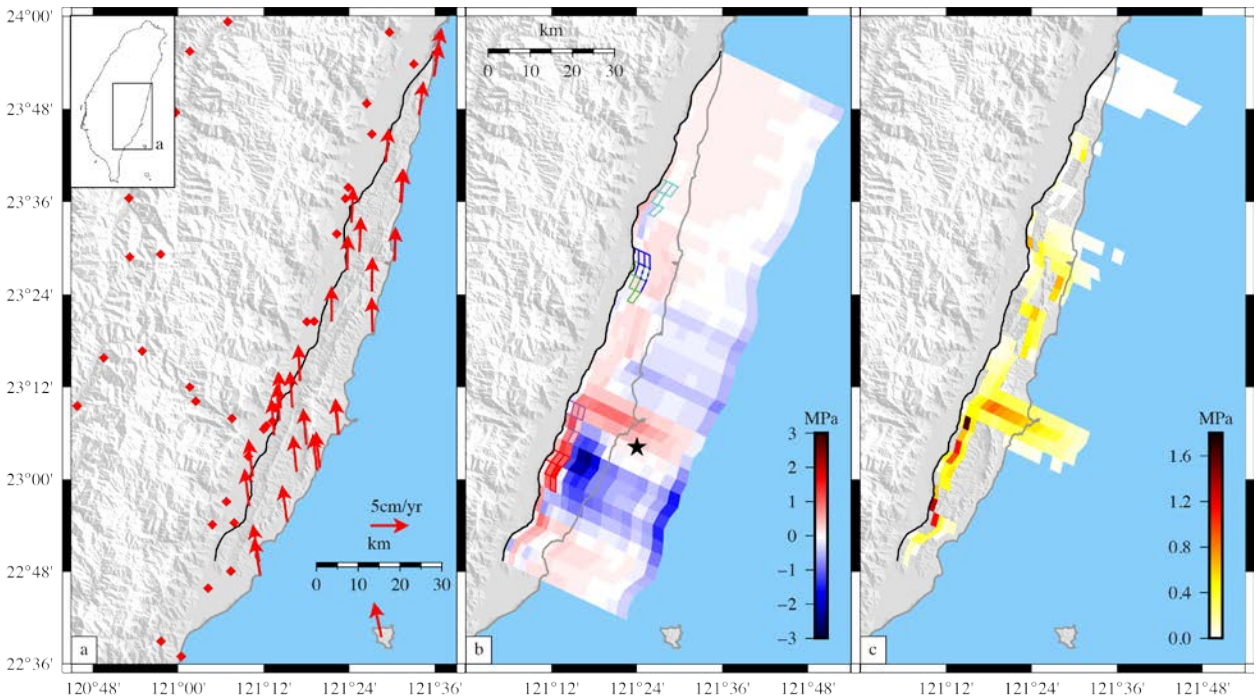

Figure S1. (a) Long-term motion of the Coastal Range (CoR) relative to the Central Range (CeR) as computed by Thomas et al., 2014a. Location of Axis and Angular Rotation Rates of the Euler Pole are defined as follows: latitude= -23.34°, longitude=-54.93° and $\Omega = 7.02°/\text{Myr}$. (b) Static Coulomb stress changes imparted by coseismic slip (Figure S2b), resolved onto the LVF fault plane for a rake corresponding to the long-term motion of the LVF. The latter is simply computed by projecting the deformation field displayed in (a), onto the fault. (c) Inferred friction parameter $(a\text{-}b)\sigma_{eff}$.

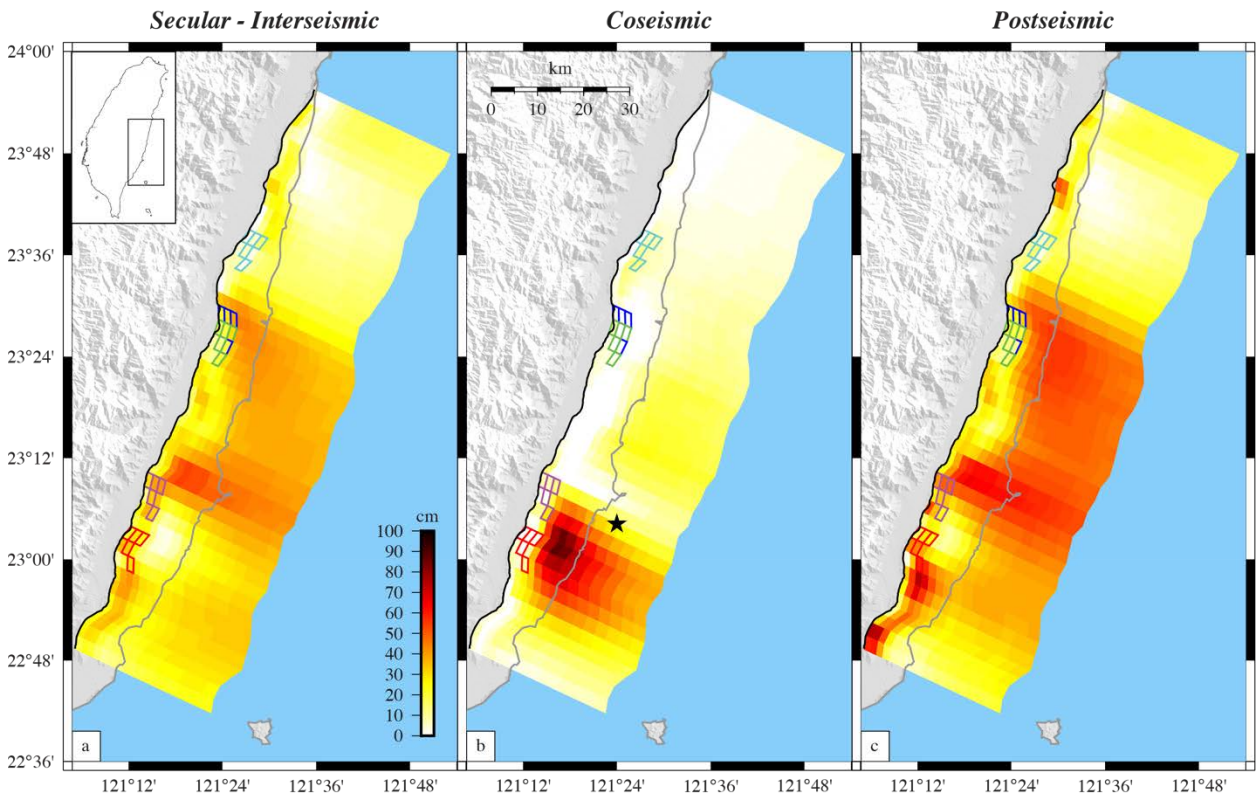

Figure S2. The three inversion models used in this study and published in Thomas et al., 2014a. (a) Secular interseismic model. The slip distribution, computed for 6.93 years, is derived from the inversion of campaign GPS data and secular interseismic velocities inferred from continuous GPS records, creepmeter secular rate, leveling data and PS ALOS mean velocities. (b) Coseismic slip distribution model of the 2003 Mw 6.8 Chengkung earthquake. This model is slightly smoother than the pre-publised one (λ = 0.007 instead of (λ = 0.005). Slip on the fault is inferred from the inversion of the static coseismic displacements determined from the GPS time series and accelerometric data. The black star indicates the epicenter of the Chengkung earthquake. (c) Postseismic slip distribution model following the Mw 6.8, Chengkung earthquake of 2003. The cumulative slip inferred for 6.96 years is determined from the inversion of GPS and creepmeter time series, leveling data and ALOS acquisitions.

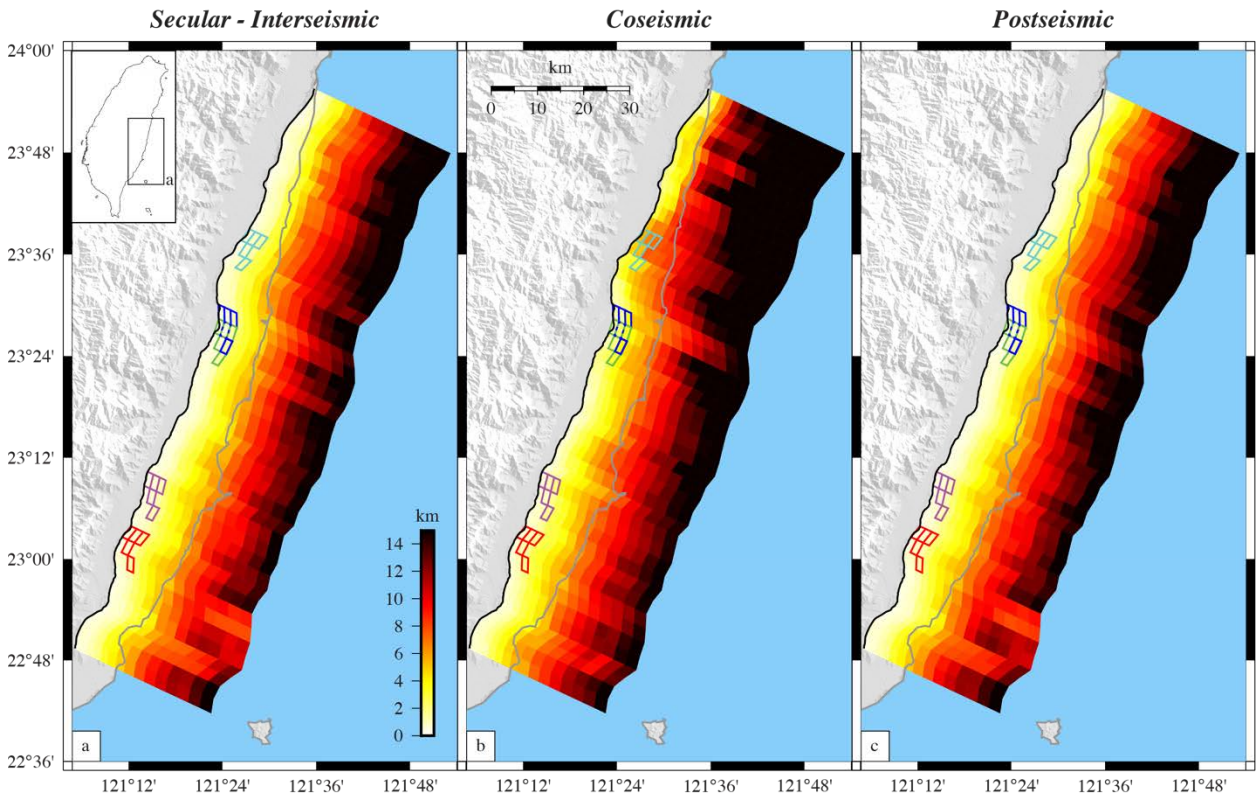

Figure S3. Resolution maps for the three inversions used in this study (Figure S2, Thomas et al., 2014). For each model, the resolution is expressed in terms of the size of the smallest inhomogeneities which could be resolved, given the distribution of data and their uncertainties. To obtain such number, at the location of each cell, we retrieve the width of the best fitting Gaussian curve at the corresponding row of the resolution matrix. These maps show that, past the coastline, the resolution on fault slip at depth becomes quite poor, as expected, given the absence of any measurements offshore but on the Ludao Island. Up-dip from the coastline, the resolution is generally smaller than 5 km and becomes as good as 511 m near the fault trace for the Interseismic model, 590 m for the Coseismic model and 509 m for the Postseismic model.

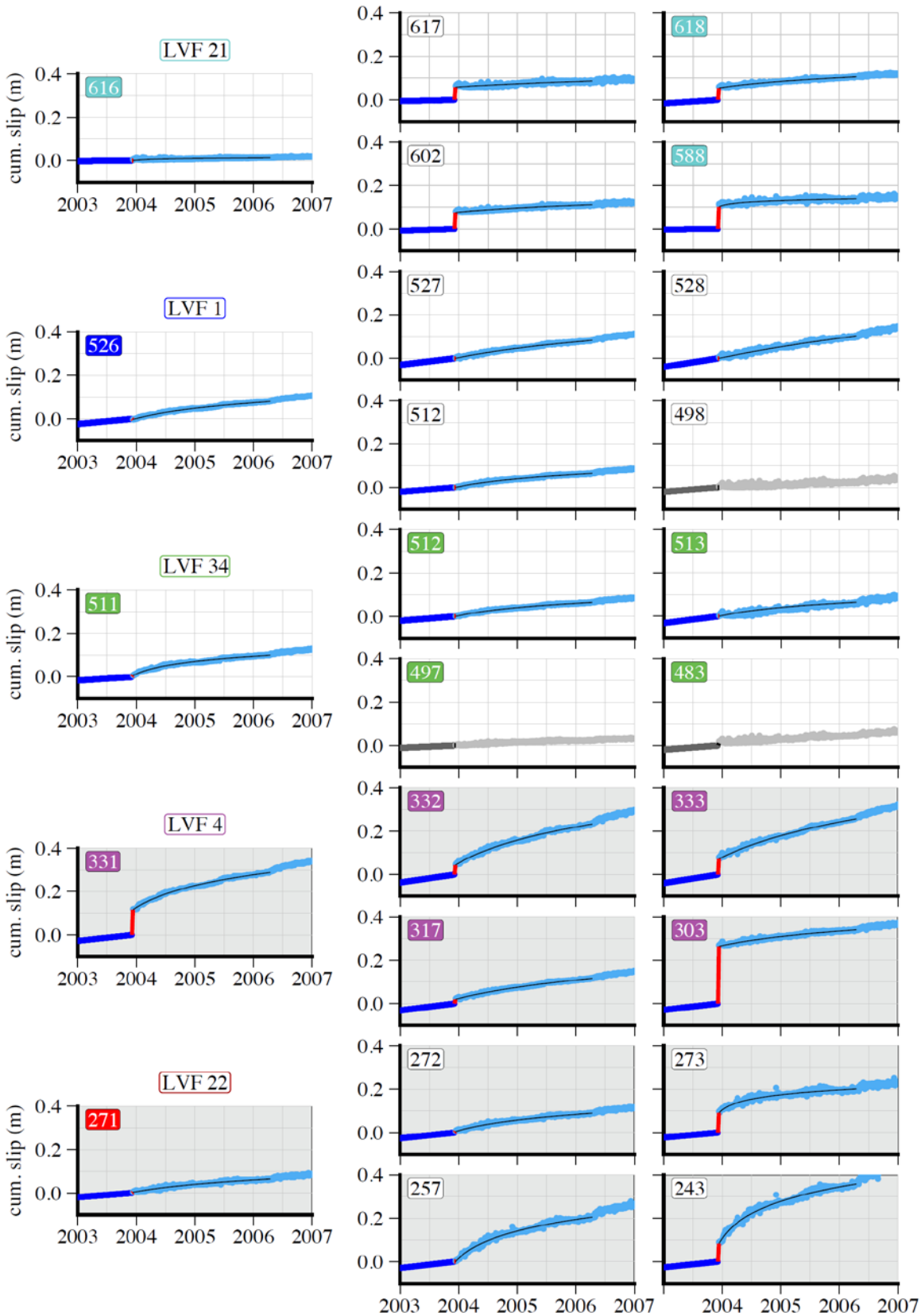
LVF 21
616
617
618
602
588
LVF 1
526
527
528
512
498
LVF 34
511
512
513
497
483
LVF 4
331
332
333
317
303
LVF 22
271
272
273
257
243
cum. slip (m)
0.4
0.2
0.0
2003
2004
2005
2006
2007

Figure S4 (previous page). Time series of slip on the fault, based on the inversions of geodetic data over the period 1997–2010 (Thomas et al., 2014a). Time evolution of slip is displayed along the direction of the long-term slip vector predicted by the block motion of the Coastal Range relative to the Central Range. Here, only data between 2003 and 2007 are provided and the location of the patches can be found in Figure 1c-f. Dark blue, red, and light blues curves represent the preseismic, coseismic, and postseismic periods, respectively. When displayed in grey, it means the friction parameters could not be inferred, either because of $\Delta CFF<0$ or because the postseismic slip rate is lower than the preseismic slip rate. Black curves correspond to the fit of the patch time series, following the relaxation law as described in equation (5). When the patch number has a background colour, it means that a laboratory measurement, at similar temperature conditions, exists. Finally, the grey background emphasizes the samples collected within a high-rate creeping zone.

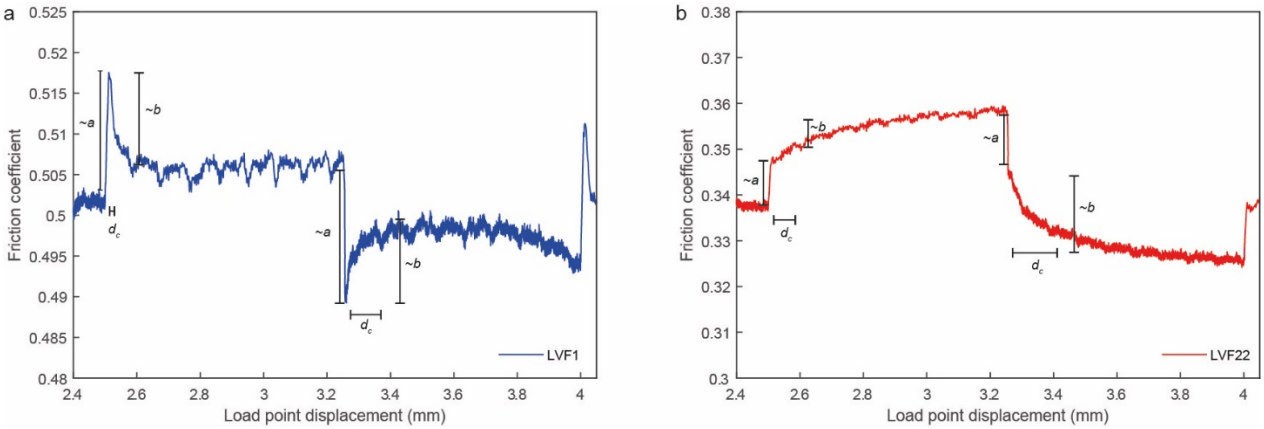

Figure S5. Close-up sections of the friction curves for samples LVF1 (a) and LVF2 (b), with the RSF parameters as obtained from the non-linear least squares numerical fitting routine. Note that the direct and evolution response are only proportional to *a* and *b* as the velocity steps applied were not equal to *e* (cf. equation 1 in main manuscript).

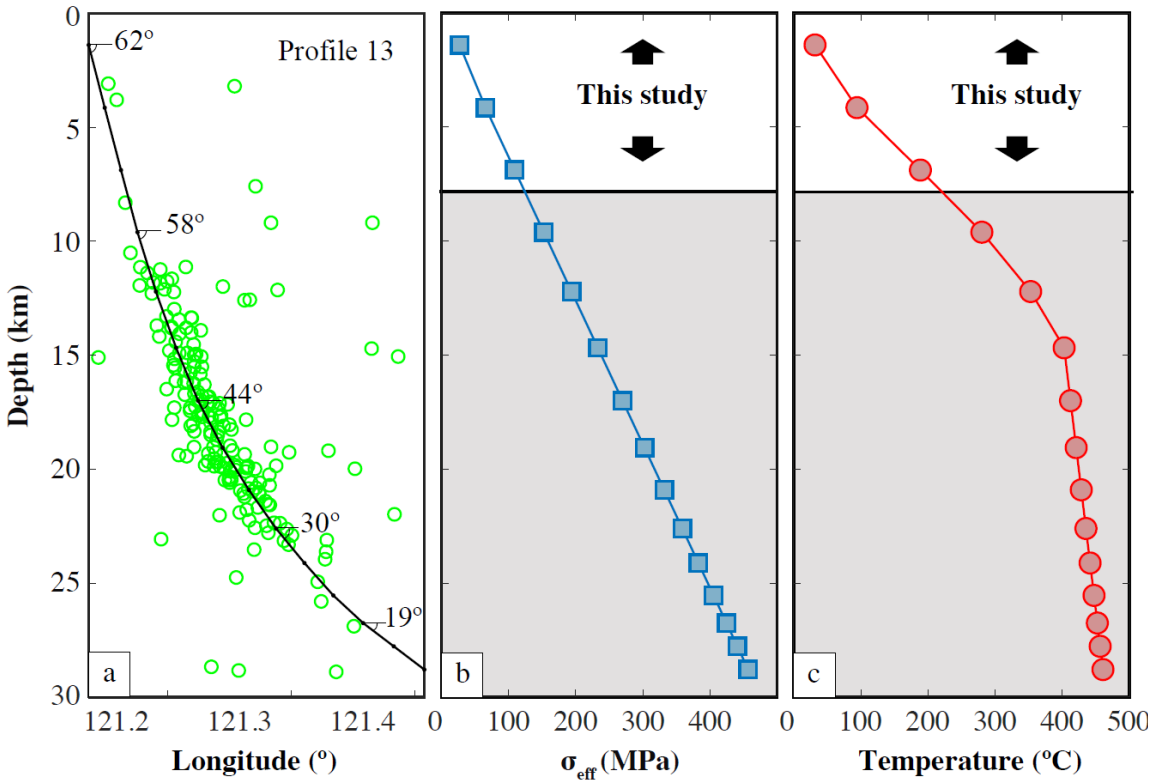

Figure S6. (a) Profile showing the variation of dip angle of the LVF with depth. Green dots correspond to the location of seismic events with magnitude $M_L > 3.2$ within a 7 km-wide swath around the profile. Location of the profile is given in Figure 1b of the main manuscript. (b) Effective normal stress distribution used for the kinematic analysis, assuming a hydrostatic pore fluid pressure and a rock density of 2700 kg/m^3. (c) Geotherm for the central part of the LVF, based on the thermokinematic model of Simoes et al. (2007).

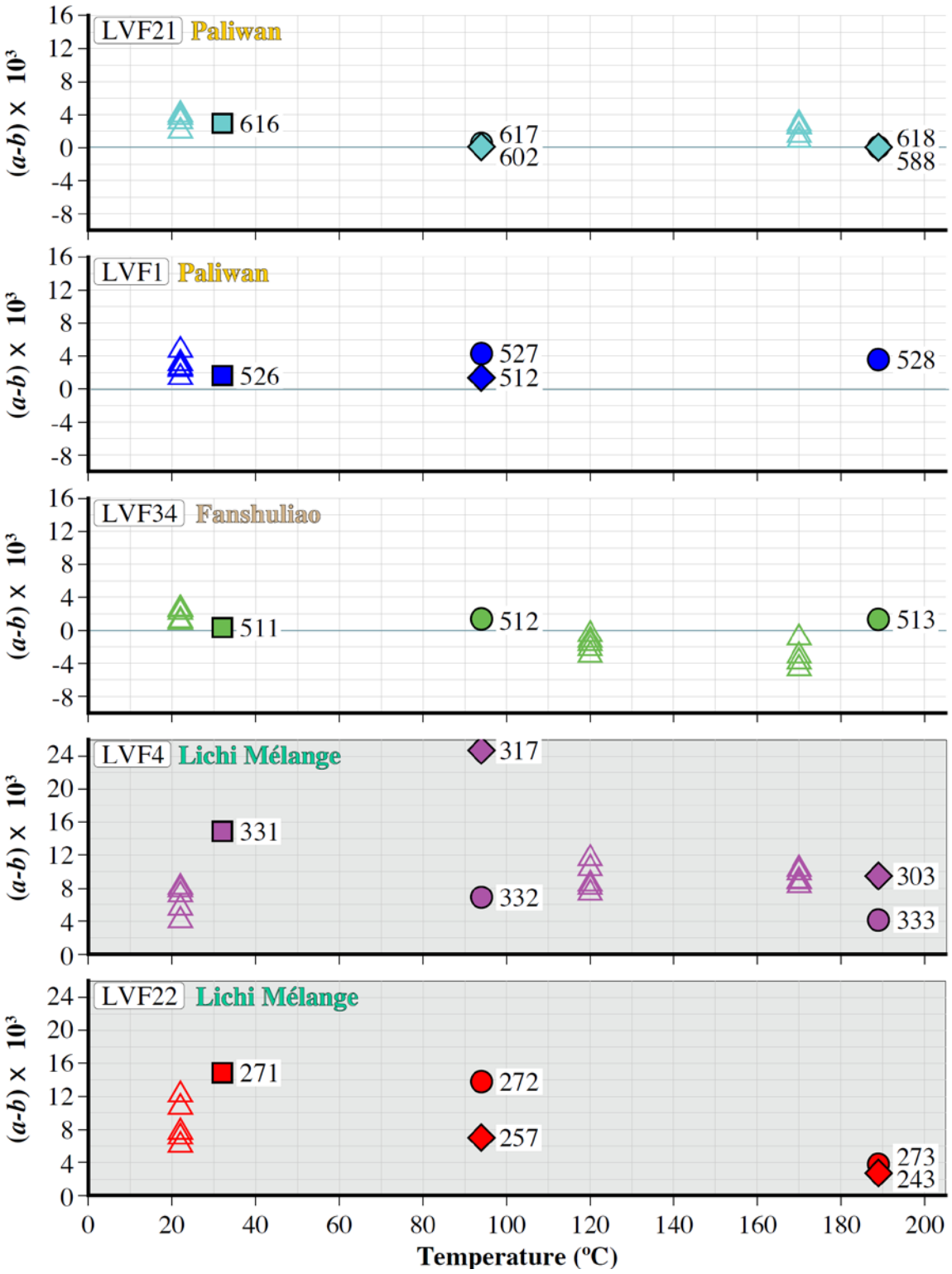

Figure S7. Variation of the friction parameter (*a-b*) with temperature for laboratory-derived data (empty triangle symbols) and inferred values using times series of slip at depth (plain symbols). For the latter, the corresponding temperature is based on the thermokinematic model of Simoes et al. (2007), as provided in Supporting Figure S6c. (*a-b*) is simply derived by dividing the data display in Figure 5 of the

main manuscript by the corresponding σ_{eff} given in Supporting Figure S6b. Square symbols correspond to the patches at the location of the samples used for experiments. Circle and diamond symbols correspond to the patches following an along-dip and a long-term slip vector profile, respectively (see Figure 1c-f of the main manuscript for location). Grey background emphasizes the samples collected within a high-rate creeping zone.

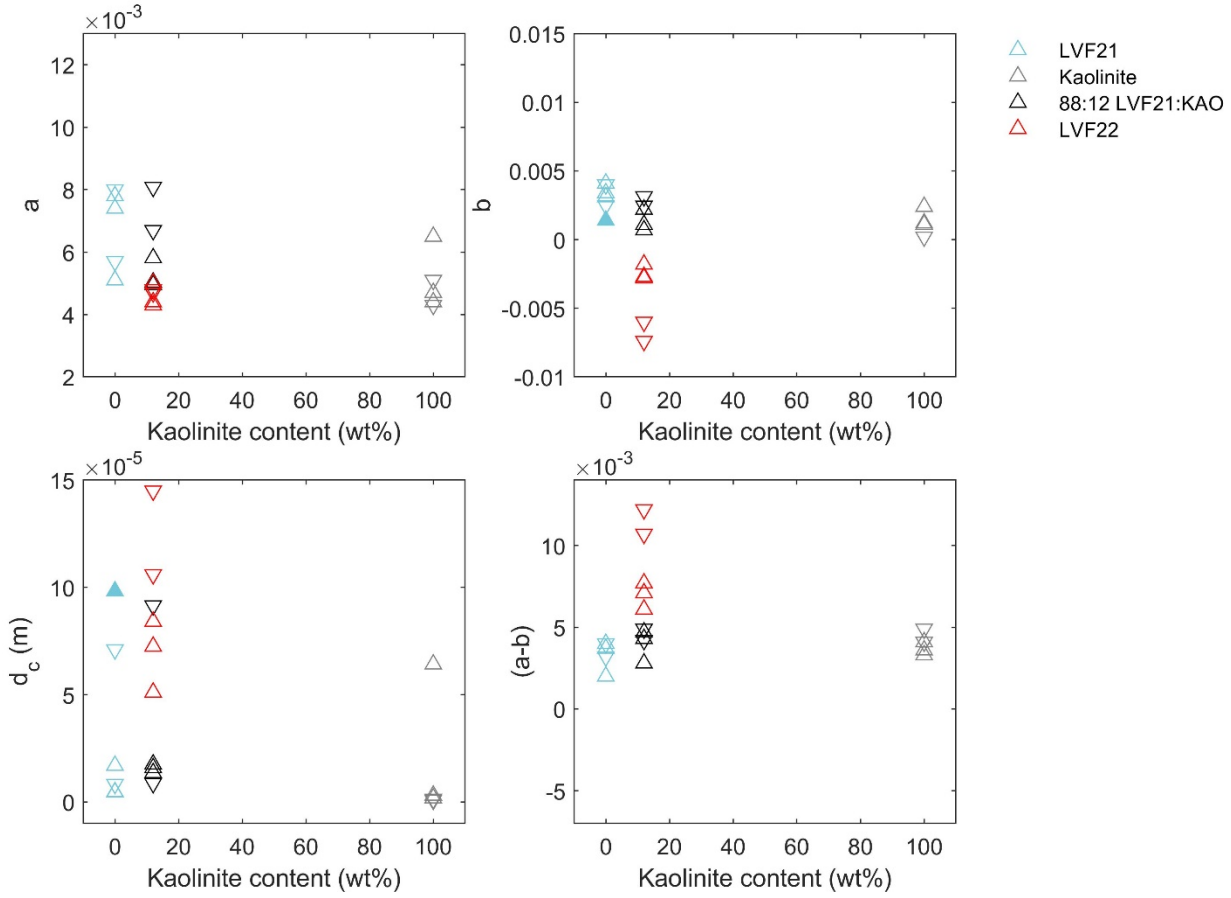

Figure S8. Rate and state friction parameters versus kaolinite content. (a) direct effect *a*, (b) evolution effect *b*, (c) critical sliding distance d_c and (d) slip stability parameter (*a*-*b*). Values for velocity steps with an increase in velocity are shown as upward pointing triangles, while values for velocity downsteps are shown as downward pointing triangles. Closed symbols represent second state variables (*b* and d_c).

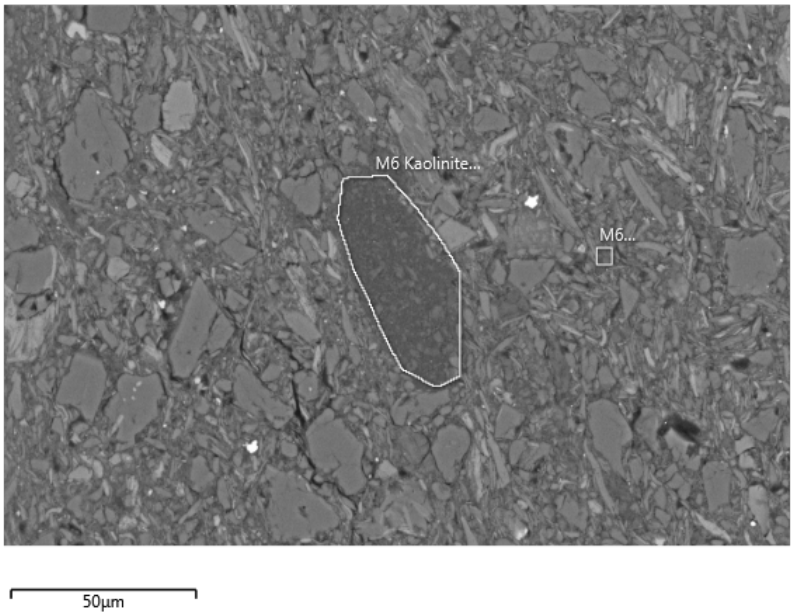

Fe At%

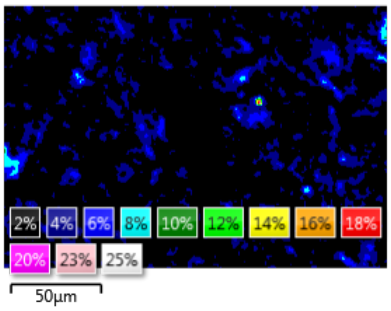

Ti At%

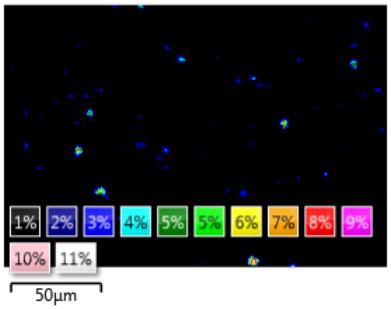

Ca At%

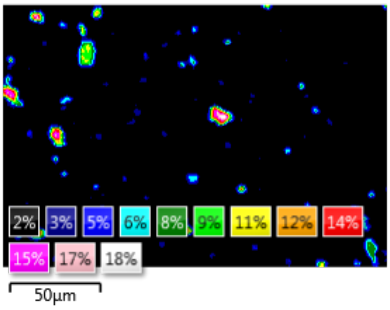

K At%

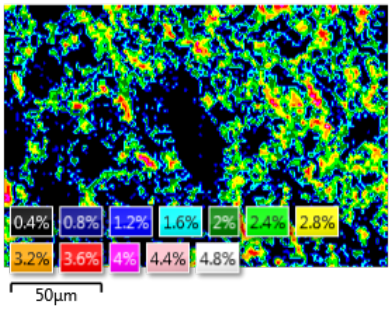

Si At%

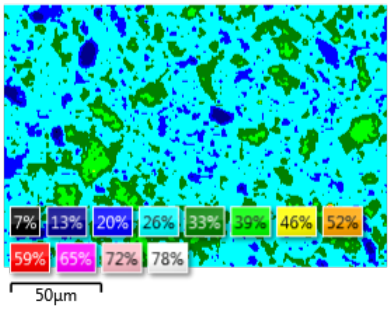

Al At%

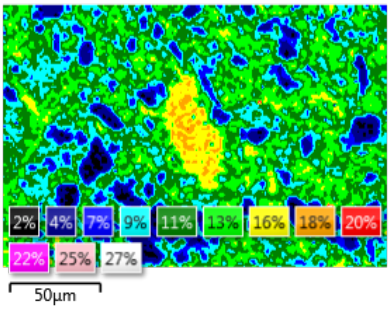

Mg At%

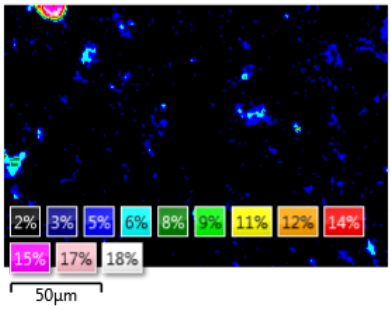

Na At%

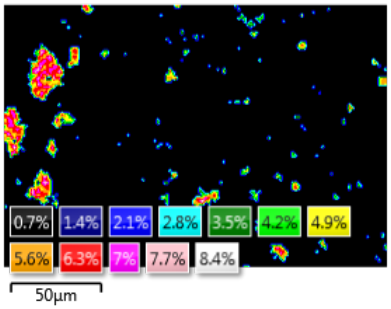

O At%

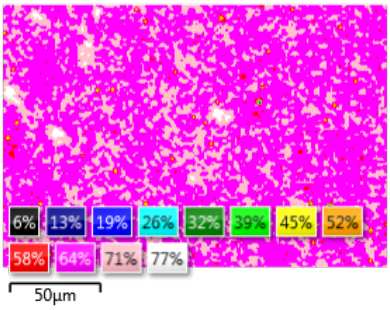

C At%

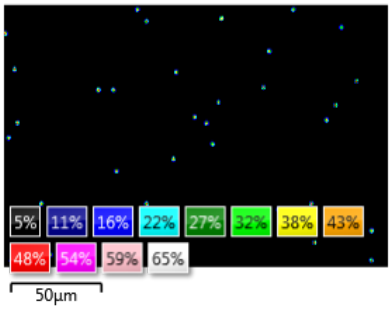

Figure S9 (previous page). Abundance of atoms as determined by Energy Dispersive X-Ray analysis for LVF21_KAO_RT. Note the central area of increased Al concentration, outlining a kaolinite cluster.

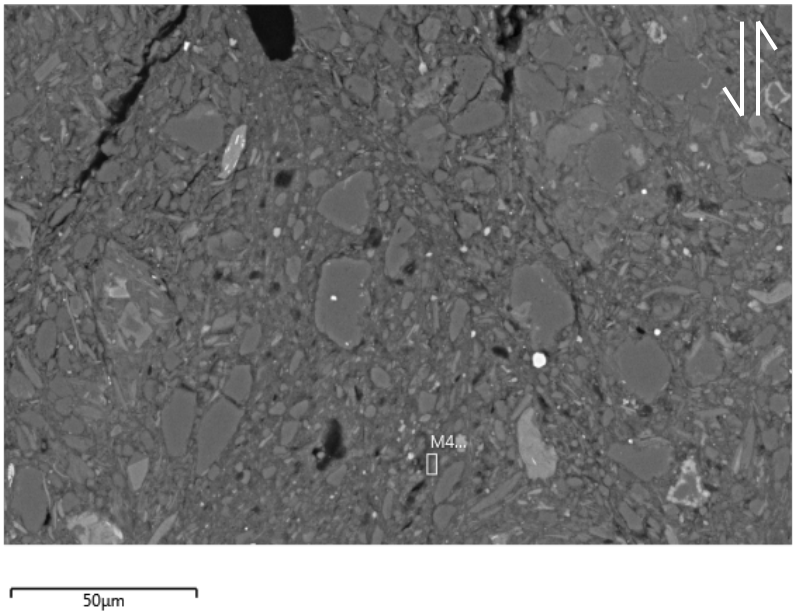

Fe At%

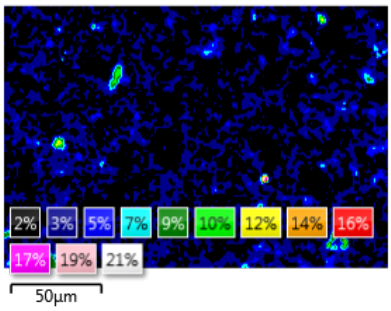

Ti At%

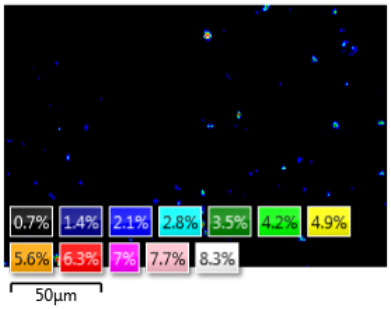

Ca At%

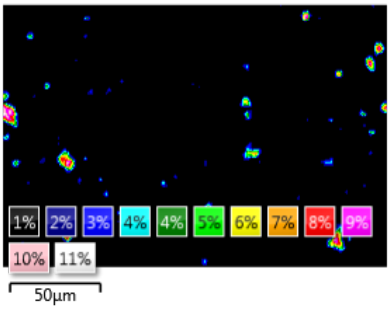

K At%

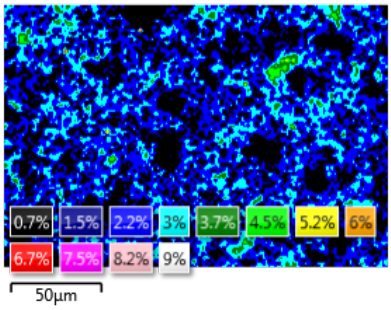

Si At%

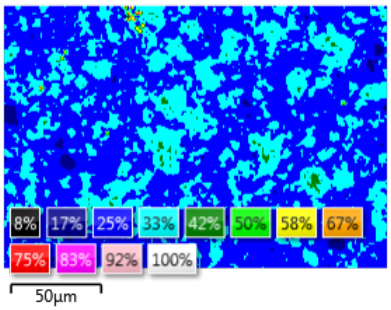

Al At%

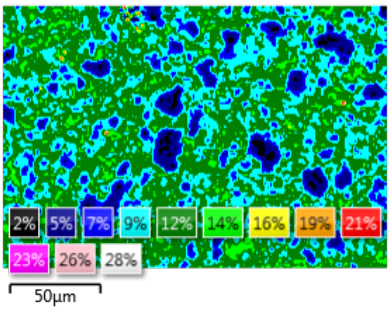

Mg At%

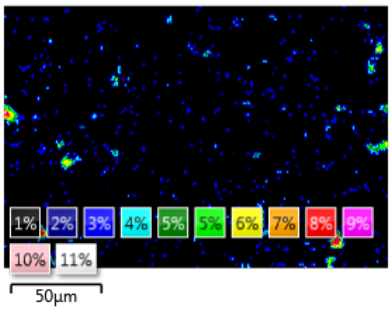

Na At%

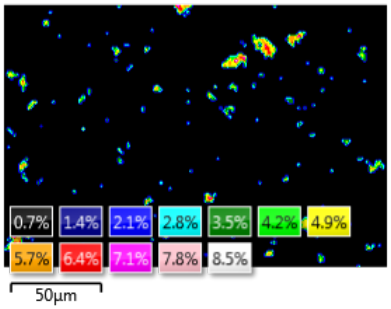

O At%

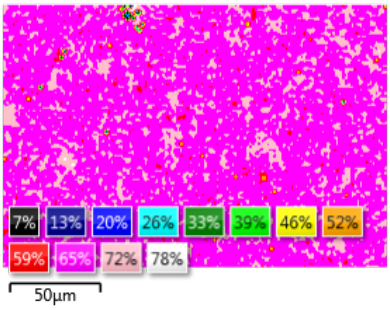

C At%

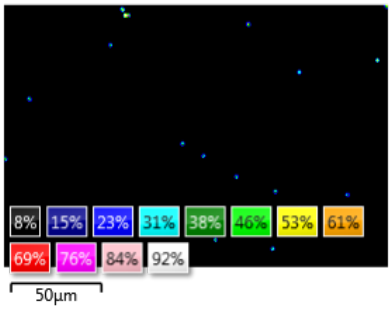

Figure S10 (previous page). Abundance of atoms as determined by Energy Dispersive X-Ray analysis for LVF22_RT. Note the absence of increased Al concentrations characteristics for kaolinite, suggesting that kaolinite is too small to be detected.

Sample	Patch #	$(a\text{-}b)\sigma_{eff}$ (MPa)	σ_{eff} (MPa)	$(a\text{-}b)$	T (°C)	Depth (km)	ISC
LVF21	616	0.08	27.1	0.0029	32	-1.39	0.96
	617	0.03	65.8	0.0005	94	-4.14	0.88
	618	0.00	109.3	0.0000	189	-6.88	0.67
	602	0.01	65.8	0.0001	94	-4.14	0.83
	588	0.01	109.3	0.0000	189	-6.88	0.96
LVF1	526	0.04	27.1	0.0016	32	-1.39	0.29
	527	0.28	65.8	0.0043	94	-4.14	0.11
	528	0.39	109.3	0.0035	189	-6.88	0.00
	512	0.09	65.8	0.0014	94	-4.14	0.45
	498		109.3		189	-6.88	0.53
LVF34	511	0.01	27.1	0.0003	32	-1.39	0.58
	512	0.09	65.8	0.0014	94	-4.14	0.45
	513	0.14	109.3	0.0013	189	-6.88	0.18
	497		65.8		94	-4.14	0.73
	483		109.3		189	-6.88	0.61
LVF4	331	0.40	27.1	0.0149	32	-1.39	0.23
	332	0.45	65.8	0.0069	94	-4.14	0.00
	333	0.46	109.3	0.0042	189	-6.88	0.00
	317	1.63	65.8	0.0247	94	-4.14	0.11
	303	1.04	109.3	0.0095	189	-6.88	0.34
LVF22	271	0.40	27.1	0.0149	32	-1.39	0.61
	272	0.91	65.8	0.0138	94	-4.14	0.47
	273	0.41	109.3	0.0038	189	-6.88	0.55
	257	0.46	65.8	0.0070	94	-4.14	0.27
	243	0.30	109.3	0.0027	189	-6.88	0.14

Table S1. List of patches from the kinematic analysis and key data. Corresponding sample names are also provided. Patch # = patch number, $(a\text{-}b)\sigma_{eff}$ = inferred $(a\text{-}b)\sigma_{eff}$, σ_{eff} = assumed effective normal stress (see Supporting Figure S2b), $(a\text{-}b)$ = friction parameter $(a\text{-}b)$, T = temperature based on the thermokinematic model of Simoes et al. (2007), Depth = depth of the centre of the patch, ISC = Interseismic Coupling (see Figure 1b of main manuscript).

Sample	T_{exp} (°C)	$[(a\text{-}b)\sigma_{eff}]_{exp}$ (MPa)	Patch #	T_{model} (°C)	$[(a\text{-}b)\sigma_{eff}]_{model}$ (MPa)	Diff	%
LVF21	22	0.20	616	32	0.08	0.12	12.2
	170	0.12	618	189	0.00	0.12	12.4
			588	189	0.01	0.11	11.4
LVF1	22	0.17	526	32	0.04	0.13	12.9
LVF34	22	0.11	511	32	0.01	0.10	10.3
	120	-0.10	512	94	0.09	-0.19	-19.0
	170	-0.19	513	189	0.14	-0.33	-32.3
LVF4	22	0.39	331	22	0.40	-0.01	-0.6
	120	0.55	332	94	0.45	0.10	10.1
			317	94	1.63	-1.08	-106.9
	170	0.55	333	189	0.46	0.09	9.4
			303	189	1.04	-0.49	-48.2
LVF22	22	0.53	271	22	0.40	0.13	12.5

Table S2. Comparison between friction parameters derived from the laboratory experiments and the kinematic analysis. Sample = sample name, T_{exp} = temperature of the experiment, $[(a\text{-}b)\sigma_{eff}]_{exp}$ = average of the different $(a\text{-}b)\sigma_{eff}$ measurement obtained from the experiments, Patch # = patch number, T_{model} = temperature based on the thermokinematic model of Simoes et al. (2007), $[(a\text{-}b)\sigma_{eff}]_{model}$ = $(a\text{-}b)\sigma_{eff}$ inferred from geodetic observations, Diff = difference between columns 3 and 6, % = difference expressed in percentage, in comparison to the range of value obtained for the laboratory data.